Article

Helical peptide structure improves conductivity and stability of solid electrolytes

Yingying Chen [1], Tianrui Xue[1], Chen Chen [1], Seongon Jang [1], Paul V. Braun [1], Jianjun Cheng [1,2] & Christopher M. Evans [1] ✉

Ion transport is essential to energy storage, cellular signalling and desalination. Polymers have been explored for decades as solid-state electrolytes by either adding salt to polar polymers or tethering ions to the backbone to create less flammable and more robust systems. New design paradigms are needed to advance the performance of solid polymer electrolytes beyond conventional systems. Here the role of a helical secondary structure is shown to greatly enhance the conductivity of solvent-free polymer electrolytes using cationic polypeptides with a mobile anion. Longer helices lead to higher conductivity, and random coil peptides show substantially lower conductivity. The macrodipole of the helix increases with peptide length, leading to larger dielectric constants. The hydrogen bonding of the helix also imparts thermal and electrochemical stability, while allowing for facile dissolution back to monomer in acid. Peptide polymer electrolytes present a promising platform for the design of next-generation ion-transporting materials.

Ion transport is central to energy storage[1–5] and signal transduction in cells[6,7]. Polyethylene oxide (PEO) has been used for decades to transport lithium and provide safer alternatives to liquid electrolytes[8,9], and most strategies to improve conductivity and stability rely on tuning polymer architecture[10–16]. New concepts are needed to push the performance of solid polymer electrolytes beyond PEO. Bulky, delocalized ionic liquid groups have been tethered to polymer backbones (polymerized ionic liquids (PILs)) to understand how ion attachment, dielectric constant, ion type and segmental dynamics (the α-process) impact conductivity[17,18]. Such approaches show great promise—for example, when both ions are attached (zwitterionic PIL) the conductivities of added lithium salts are massively enhanced for a given rate of segmental dynamics, leading to 'superionic' behaviour[19] and emphasizing the important role of ionic architecture.

The helix is ubiquitous in biology (for example, DNA) and leads to unique chemical, physical and mechanical properties[20]. This structure is also of vital importance in drug and gene delivery[21], energy storage[22–25] and antimicrobials[26,27]. Recently, α-helical polypeptides with two redox active groups were developed as anode and cathode materials for electron conduction in all-organic, metal-free secondary batteries. These peptides showed excellent electrochemical stability and on-demand degradability[28], but the role of the helical structure was not investigated. Although PEO can form a helical structure, this only occurs in the crystalline state where conductivity is low[29]. Peptides, derived from the ring-opening polymerization (ROP) of N-carboxyanhydrides (NCAs), are ideal materials for understanding how helical architecture can lead to favourable pathways for ion transport in the molten state and stabilize polymers to external conditions by controlling secondary structures using NCAs with the same chemistry but different chirality (L and D), leading to analogous random coil or helical polypeptides[30]. This approach is distinct from inducing conformational transitions in peptides via pH which leads to changes in the charge of side groups and polarity which can affect ionic conductivity.

[1]Department of Materials Science and Engineering, Materials Research Laboratory, Beckman Institute for Advanced Science and Technology, University of Illinois Urbana-Champaign, Urbana, IL, USA. [2]School of Engineering, Westlake University, Hangzhou, China. ✉e-mail: cme365@illinois.edu
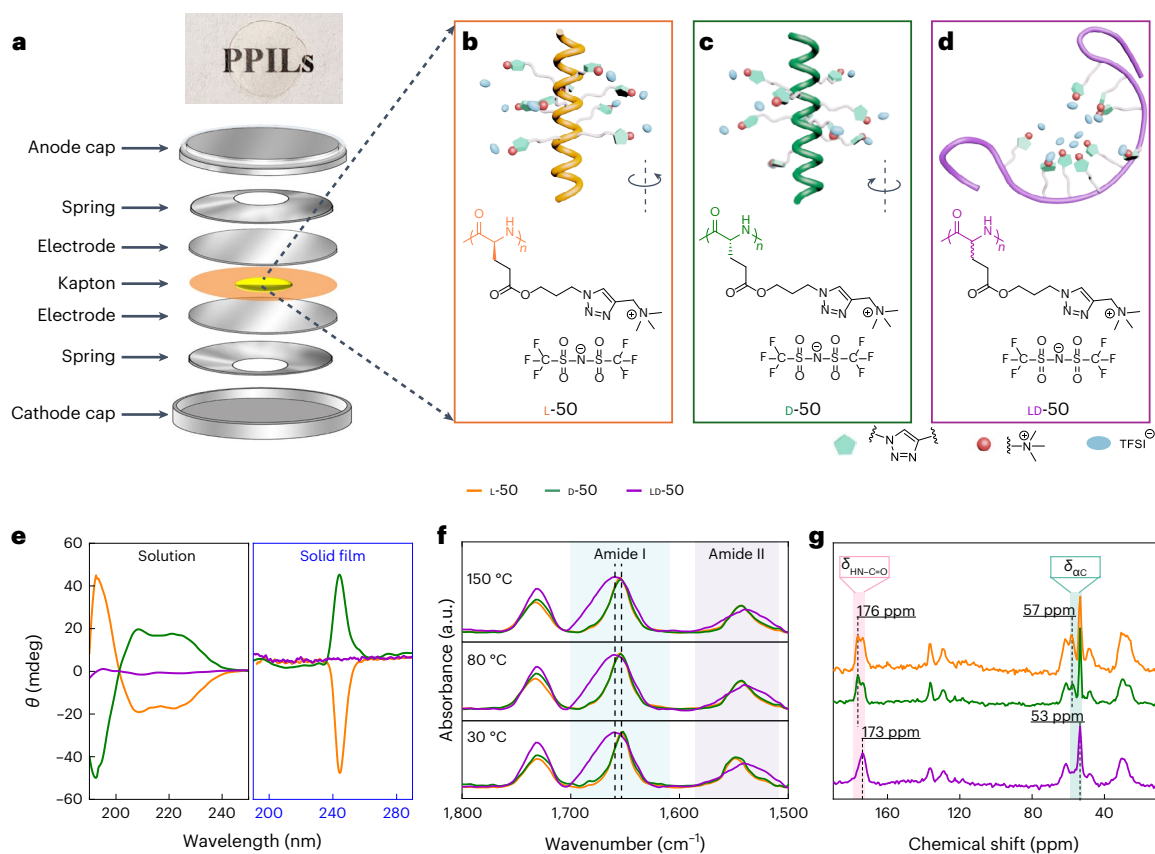
Fig. 1 | Synthesis and conformation of helixes in the solid state. a, Schematic illustration of coin cell assembly and an image of a transparent PPIL hot-pressed film. **b–d**, Illustration of the secondary structure and chemical structure of PPILs (x-50s): L-50 adopted a right-handed α-helical conformation (**b**); D-50 exhibited a left-handed helical conformation (**c**); and LD-50 displayed a random coil conformation (**d**). **e**, CD spectra of x-50s in solution (0.5 mg ml^{-1} in methanol)

and solid films. **f**, ATR-FTIR spectra of x-50s at different temperatures with equilibration times of 10 min. The vertical lines correspond to the amide I peak for random coils (1,661 cm^{-1}) and the helical structure (1,652 cm^{-1}). **g**, CP-MAS ^{13}C NMR spectra of x-50s. The different colour curves correspond to L-50 (orange), D-50 (green) and LD-50 (purple).

Helical polypeptide PILs (PPILs) were designed and synthesized to demonstrate how secondary structure improves the ionic conductivity and stability relative to analogous random coil electrolytes. Three PPILs (x-DP, where x and DP denote the chirality and the degree of polymerization, respectively) were synthesized with the same chemical formula and DP, but with either helical or random coils (Fig. 1a–d). The as-cast random coil PPIL exhibited a substantially higher glass transition temperature (T_g) but annealing at 473 K disrupts unstable hydrogen bonding and lowers T_g. Helical PPILs show higher conductivity than the PPILs with random coils and no change in conductivity or T_g due to the stability of the helix. The enhanced conductivity of helical PPILs can be further improved by increasing the DP because the persistent direction of the helical backbone creates a macrodipole that directs ionic transport, increases the dielectric constant and leads to substantially higher conductivity than random coils. All PPILs are stable over a 6 V window, and can be degraded to the starting amino acid and other well-defined products, reducing the environmental impact of peptide electrolytes. This work demonstrates the key role of secondary structure on ionic conductivity and stability as a new design concept in solid polymer electrolytes.

Polypeptides with different secondary structures
Three polypeptides were synthesized (Supplementary Scheme 1) by the controlled ROP of γ-(3-chloropropanyl)-x-glutamate NCA (CIPxG-NCA) made from L-, D- and LD-glutamic acids (xGs). Polypeptides with DP = 50 and low dispersity (*Đ* < 1.1) were confirmed by size exclusion chromatography (SEC) and ^{1}H NMR (Supplementary Figs. 1–6). PCIPLG and

PCIPDG adopted a right-handed and left-handed helix, respectively, as evidenced by the absorbance peaks of amide I at 1,652 cm^{-1} and amide II at 1,548 cm^{-1} in Fourier transform infrared spectra (FTIR) and the double minima/maxima at 208 nm and 222 nm via circular dichroism (CD). PCIPLDG adopted a random coil conformation based on the shift in the amide I absorption peak at 1,661 cm^{-1} and negligible intensity in the CD spectra (Supplementary Fig. 7). Functionalization of the side chains provided the final PPILs (x-50s) with ammonium-bis(trifluoromethane) sulfonamide (TFSI) ion pairs, including azidation of the chloro group, copper-catalysed azide–alkyne cycloaddition (CuAAC) click reaction to incorporate charged groups, and finally ion exchange (Supplementary Table 1). The resulting polymers have tethered ammonium groups and mobile TFSI groups which are responsible for the conductivity. PPILs were freeze-dried and then vacuum dried at 393 K for at least 2 days to remove water, and the DP was unchanged from the starting peptides (Supplementary Figs. 8–10).

The secondary structures of L-, D- and LD-50 PPILs were maintained based on FTIR (Supplementary Fig. 11) and CD spectra in methanol (Fig. 1e, left). Secondary structure differences in the solid state were confirmed by ATR-FTIR, CD and cross-polarization magic-angle spinning (CP-MAS) solid-state ^{13}C NMR spectroscopy. Films (~100 μm) were hot-pressed at 80 °C, and the FTIR spectra show amine I at 1,653 cm^{-1} and amine II at 1,548 cm^{-1} for L-50 and D-50, indicating the helix is maintained in the solid state (Fig. 1f). LD-50 adopted a random coil conformation (amide I peak at 1,661 cm^{-1}). No peak is observed for LD-50 in the CD spectra (Fig. 1e), while mirror peaks appeared between 240 nm to 250 nm for L-50 and D-50, indicating opposite handed helices.
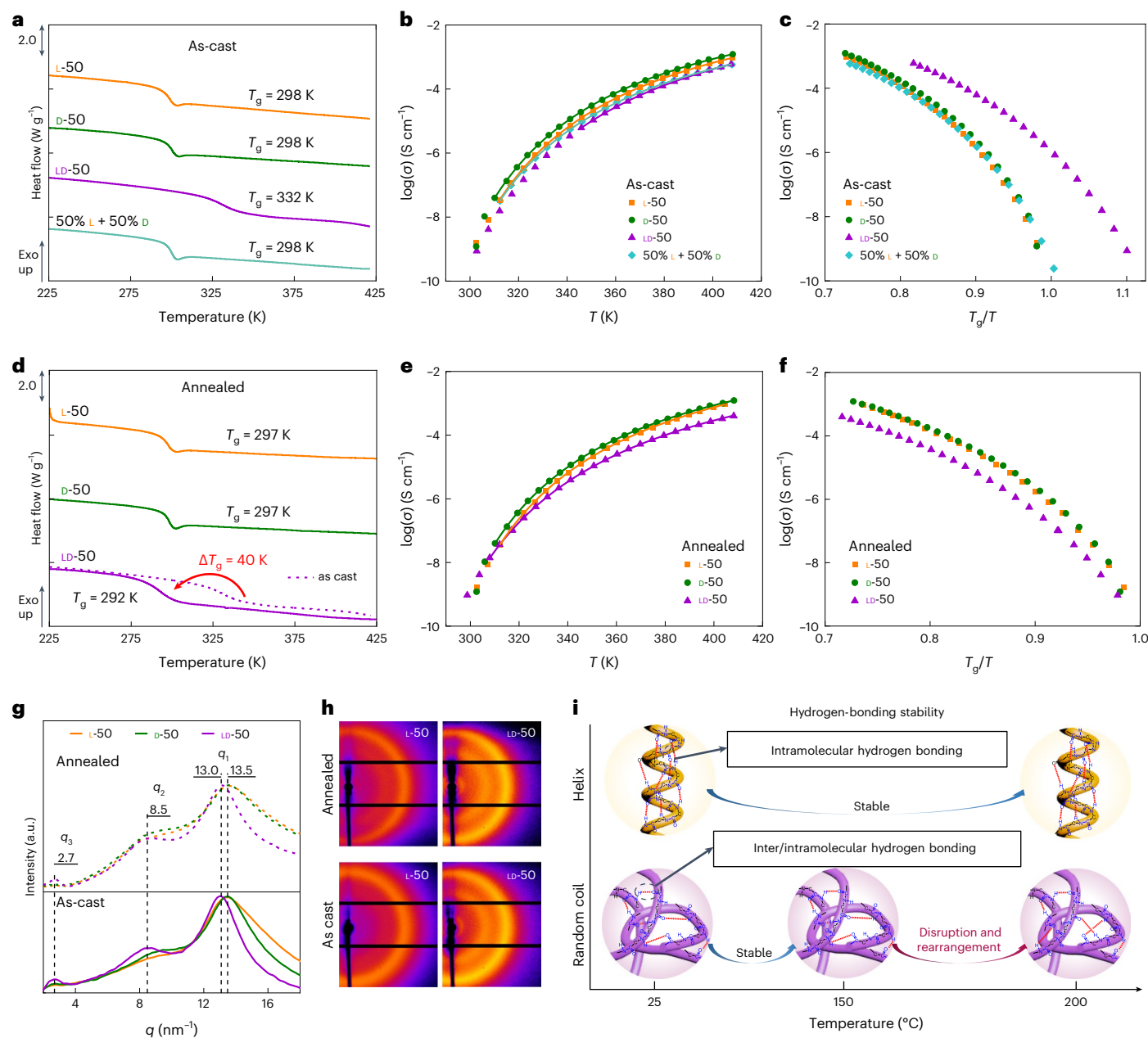
Fig. 2 | Temperature and thermal history effects on conductivity and stability. a, Second heat cycle DSC curves of as-cast x-50s under N_2 flow from −60 to 150 °C at a heating and cooling rate of 10 °C min⁻¹. **b,c**, Ionic conductivities of as-cast x-50s as a function of temperature (**b**) and as a function of T_g/T (**c**). **d**, Second heat cycle DSC curves of 473 K annealed x-50s. **e,f**, Ionic conductivities of 473 K annealed x-50s as a function of temperature (**e**) and as a function of T_g/T (**f**). **g**, WAXS profiles of as-cast (bottom, solid lines) and 473 K annealed (upper, dashed lines) x-50s. **h**, 2D WAXS patterns of as-cast and 473 K annealed L-50 and LD-50. **i**, Schematic showing a proposed mechanism for hydrogen-bonding stability during thermal processing.

The conformation-dependent ^{13}C chemical shift of C_α and amide C=O was measured by CP-MAS solid-state ^{13}C NMR[31] (Fig. 1g), and both L-50 and D-50 have a carbonyl signal at 176 ppm and C_α at 57 ppm corresponding to a helical conformation. These two signals shift downfield by 3 and 4 ppm, respectively, in LD-50, indicating a random coil conformation[32]. The width of these two peaks was broadened in LD-50, corresponding to more heterogeneity in the local environment. Thus, the L-50 and D-50 are helical while LD-50 is a random coil from a combination of FTIR, CD and NMR. An equimolar mixture of 50% L-50 + 50% D-50 (Supplementary Fig. 12) was prepared as a comparison by physical mixing and dissolution, followed by casting and drying. The only difference in the various PPILs is the secondary structure, and thus its role on ion transport can be elucidated.

Helical structure stabilizes PPILs

The degradation temperatures (T_d) and T_g were measured by thermal gravimetric analysis (TGA) and differential scanning calorimetry (DSC), respectively (Supplementary Table 2). Helical L-50 and D-50 showed high T_d = 591 K and 598 K, respectively, while LD-50 is less stable with T_d = 556 K (Supplementary Fig. 13). The as-cast helical PPILs showed the same T_g (297–298 K) because the direction of the helix does not affect segmental dynamics, while the as-cast random coil PPIL exhibited a higher T_g = 332 K (Fig. 2a). The origin of T_g in peptides is attributed to the motion of side chains because the helix is relatively static[31,33]. After annealing at 473 K, no change occurred in the stable helical peptides, while T_g dropped by 40 K to 292 K in the random coil and became broader (Fig. 2d). No degradation was detected by NMR
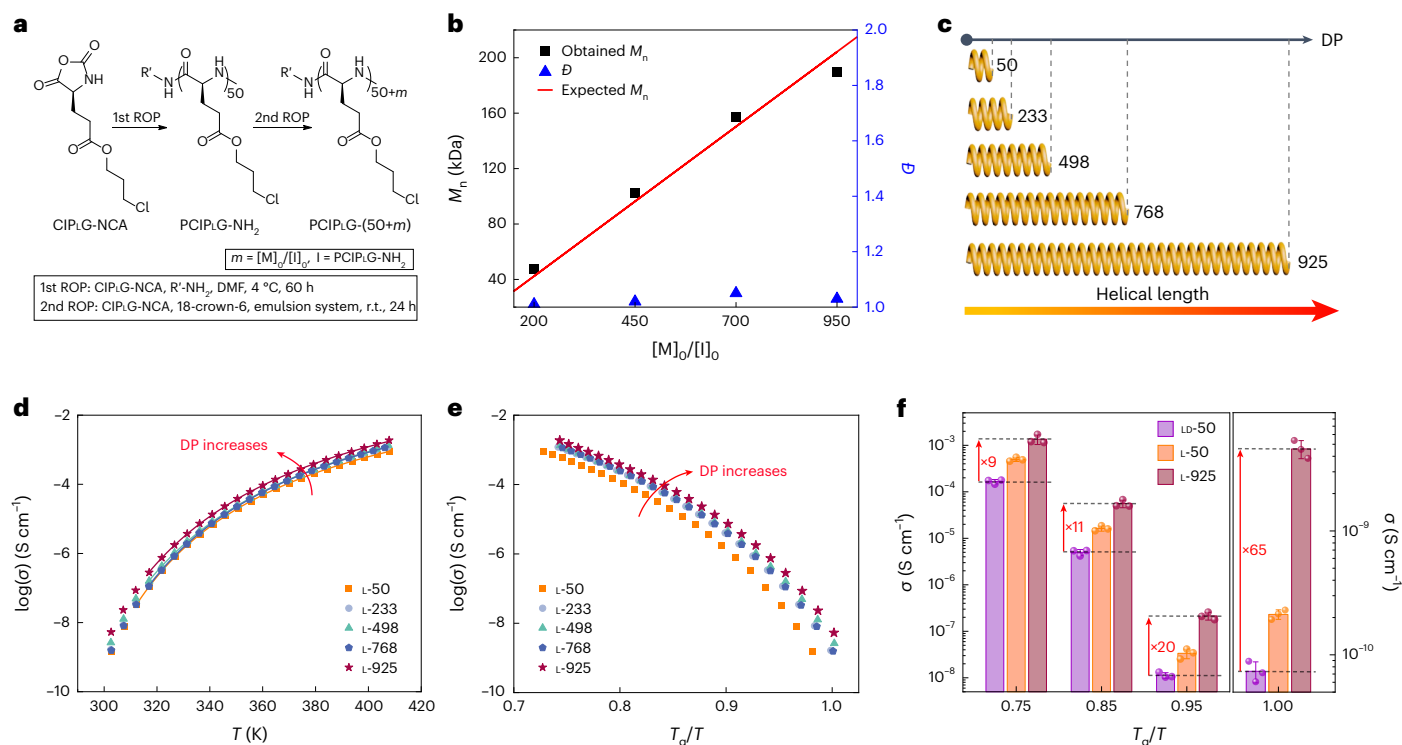
Fig. 3 | Role of increasing helix length on increased conductivity. a, Construction of polypeptide backbones with higher helical length by a two-step process: hexylamine-initiated ROP to synthesize the α-helical macroinitiator PCIPLG$_{50}$-NH$_2$, followed by a second ROP in a dichloromethane/phosphate buffer emulsion (V_{DCM}/$V_{pH7\ phosphate\ buffer}$ = 95%/5%) with different feeding ratios [M]$_0$/[I]$_0$. **b**, Comparison of the expected MWs, obtained MWs and $Đ$ of polypeptide backbone PCIPLG- (50+m) initiated by PCIPLG$_{50}$-NH$_2$. **c**, Schematic representation of the growth of helical length with increasing DP. **d,e**, Ionic conductivities of L-DPs as a function of temperature (**d**) and T_g/T (**e**). Solid curves are VFT fits. **f**, Enhancement of conductivity due to the helix at various temperatures above (left) and equal to (right) T_g. Data are means ± s.d., n = 3 independently prepared replicates. The effect grows from an order of magnitude to a factor of 65 at lower temperatures.

and FTIR (Supplementary Fig. 14). Helices are formed and stabilized through intramolecular hydrogen bonding between C=O and N–H groups on the same backbone, but random coils do not have regular hydrogen-bonding patterns and are less stable (Fig. 2i). Five DSC heating cycles (Supplementary Fig. 15) were used to analyse the stability of LD-50, and at 473 K an endotherm is observed only on the first heating and attributed to the disruption and restructuring of hydrogen bonds leading to a T_g drop with subsequent heating cycles. Helical PPILs do not show any additional thermal transitions or shifts in T_g with heating up to 473 K. ATR-FTIR spectroscopy of LD-50 after annealing (Supplementary Fig. 16) revealed that amide I peak is broadened, but can be reversed to the original state by redissolving and then drying, and the changes are not due to thermal degradation which occurs at 513 K. Helical peptides show no change in ATR-FTIR upon annealing. Peptides made via solid-phase synthesis would provide key insights into the potential role of short chains on the metastable hydrogen bonding in LD-50, as would mixtures of random coil and helical PPILs.

Helical structure promotes ionic conductivity

Electrochemical impedance spectroscopy (EIS) was used to measure the ionic conductivity from 298 K to 408 K; all samples were measured in triplicate and errors determined from the standard deviation of Vogel–Fulcher–Tammann (VFT) fit parameters from three independent samples (Supplementary Table 2 and Supplementary Figs. 17 and 18). FTIR spectroscopy indicates the stability of both helix and random coil conformations at various temperatures (Fig. 1f and Supplementary Fig. 19). A non-Arrhenius conductivity was observed for all PPILs as expected for ionic polymers. Conductivities are shown in Fig. 2 (Supplementary Figs. 20–22), and as-cast and annealed helical PPILs exhibited higher ionic conductivity at fixed temperature compared to

random coils with the same thermal history (Fig. 2b,e). To confirm that helical peptides are single-ion conductors, a lithium-conducting analogue was synthesized (Supplementary Schemes 2 and 3) and the transference number was measured as $t_{ss}^+ = 0.93 \pm 0.05$ (Supplementary Figs. 23–25). The T_g-normalized ionic conductivity of as-cast LD-50 (Fig. 2c) is higher than that of the helices due to the initially higher T_g of the sample which drops upon annealing due to unstable hydrogen bonding. Annealed helical PPILs (Fig. 2f) are ultimately more conductive at a given temperature, before and after T_g-normalization, and are stable when annealed. This points to the critical role of thermal history when considering peptides for energy applications.

To better understand the conductivity of PPILs, data at T_g + 10 K and above were fitted with the VFT equation:

$$\sigma(T) = \sigma_\infty \exp\left(-\frac{DT_0}{T - T_0}\right) \tag{1}$$

where σ_∞ is the theoretical limiting ionic conductivity at high temperature, D is the strength parameter (describing a non-Arrhenius character), and T_0 is the Vogel temperature where the ionic conductivity hypothetically diverges to zero[34,35]. Fitting parameters are summarized in Supplementary Table 2. As-cast and annealed L-50s and D-50s (entries 1–4) indicate that conductivity is independent of helical direction, and the helix is stable up to 473 K. Obvious differences between helical and random coil PPILs (entries 1–7) indicate the major role of thermal history on unstable random coil hydrogen bonding (entries 5 and 6).

Nanoscale morphology of PPILs

Small-angle and wide-angle X-ray scattering (SAXS/WAXS) were used to investigate the morphology of the PPILs (Fig. 2g–h). No long-range
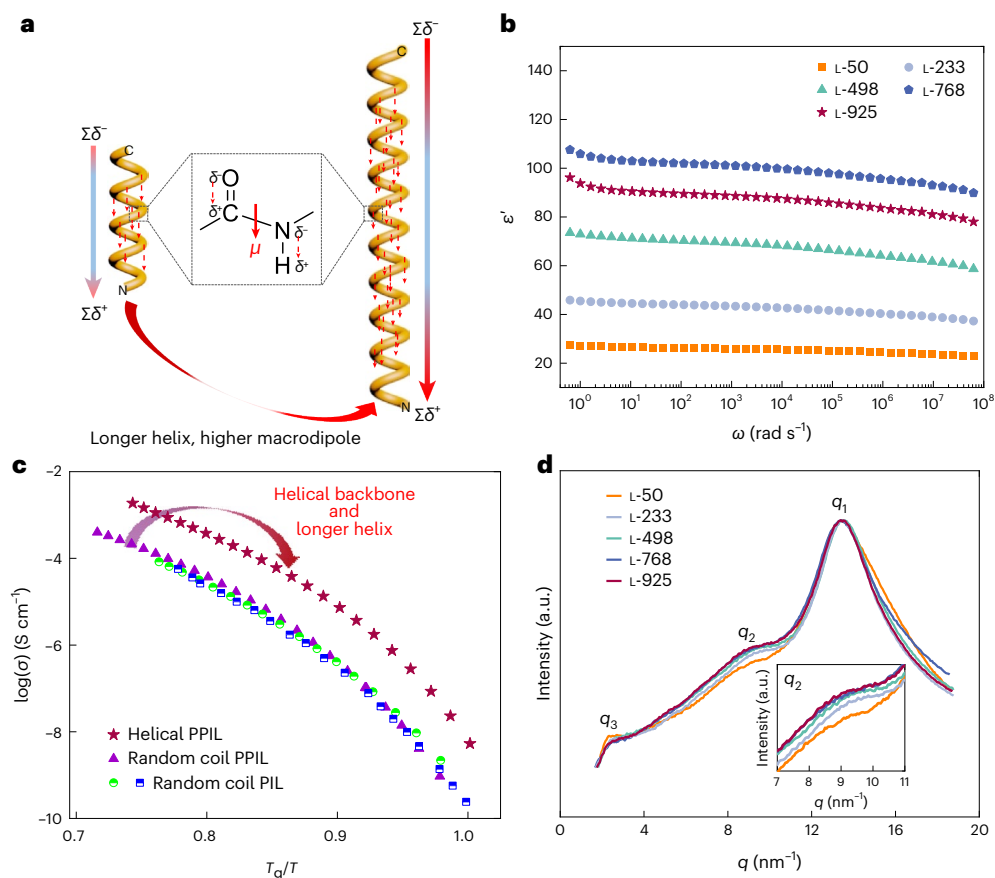
Fig. 4 | Longer helices increase macrodipole, dielectric constant and conductivity. a, Scheme showing the macrodipole of a helix. **b**, The dielectric spectra ε' of L-DPs at 243 K. **c**, Comparison of the T_g-normalized ionic conductivity of helical and random coil PPILs (L-925 and LD-50), and of previously studied random coil PILs with similar ion pairs from Zhao et al.[50] (green) and Fan et al.[40] (blue). **d**, Normalized WAXS profiles of L-DPs.
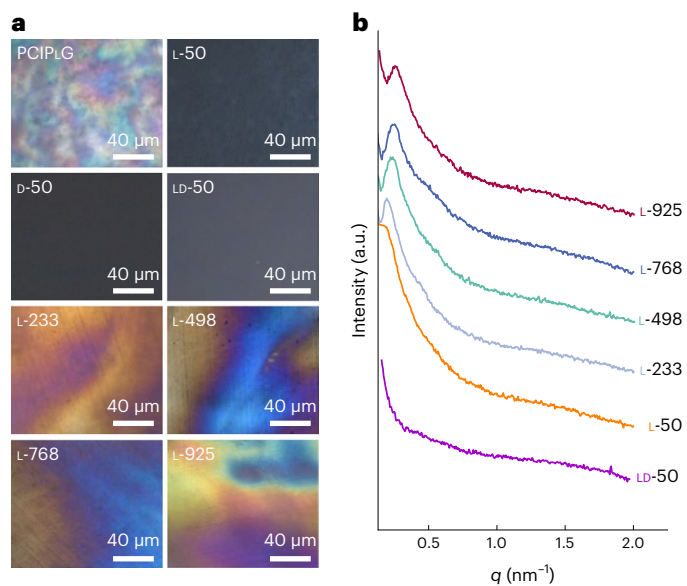

Fig. 5 | Liquid crystallinity at PPIL surfaces. a, POM images of precursor PClPLG and x-DP hot-pressed films. **b**, GISAXS profiles of L-DPs and LD-50 hot-pressed films at an angle of incidence of 0.15°.

order was observed (Supplementary Fig. 26), and no peaks associated with the secondary structure are discernible from the amorphous halo. However, FTIR, CD and ^{13}C NMR are sufficient to demonstrate that the secondary structure is different (Fig. 1). Thermal annealing has no

impact on helical L-50 and D-50, but a noticeable effect on LD-50. Based on previous PIL studies[36–38], the highest peak (q_1) was assigned as the amorphous halo, the intermediate peak (q_2) reflects ion–ion correlations, and the lowest peak (q_3) corresponds to backbone–backbone correlations. Helical PPILs showed a broad amorphous halo at $q_1 \approx 13.5 \text{ nm}^{-1}$, while LD-50 exhibited a substantial shift to $q_1 \approx 13.0 \text{ nm}^{-1}$. As-cast LD-50 showed $q_2 = 8.5 \text{ nm}^{-1}$, lower than L-50 and D-50 with $q_2 = 9.4 \text{ nm}^{-1}$, indicating that the initial hydrogen bonding of LD-50 can lead to longer-range ionic correlations of the TFSI anions, an increase in T_g and greater decoupling of conductivity from segmental dynamics prior to annealing. Peak q_3 is also lower in as-cast LD-50, indicating longer-range correlations for ion transport. After annealing, the hydrogen bonding was disrupted and the intensity of peaks q_2 and q_3 in LD-50 decreased, corresponding to a decrease in ionic conductivity. The changes in peak intensity are only discussed qualitatively because many factors affect the scattering, but all systems possess the same backbone and ions, making qualitative changes meaningful.

Synthesis and characterization of helical PPILs with increasing lengths

The role of the helix on efficient ion transport was further investigated by increasing the length of right-handed PPILs. The hypothesis is that increasing the macrodipole will direct ion transport over longer length scales and increase the dielectric constant. A crown-ether-catalysed ROP method enables the production of polypeptides with extremely high molecular weights (MWs)[39]. A helical macroinitiator PClPLG$_{50}$-NH$_2$ (Fig. 3a and Supplementary Fig. 27) was synthesized by hexylamine initiation at 4 °C to maintain the end amine group fidelity. A second ROP in a dichloromethane/phosphate buffer emulsion system
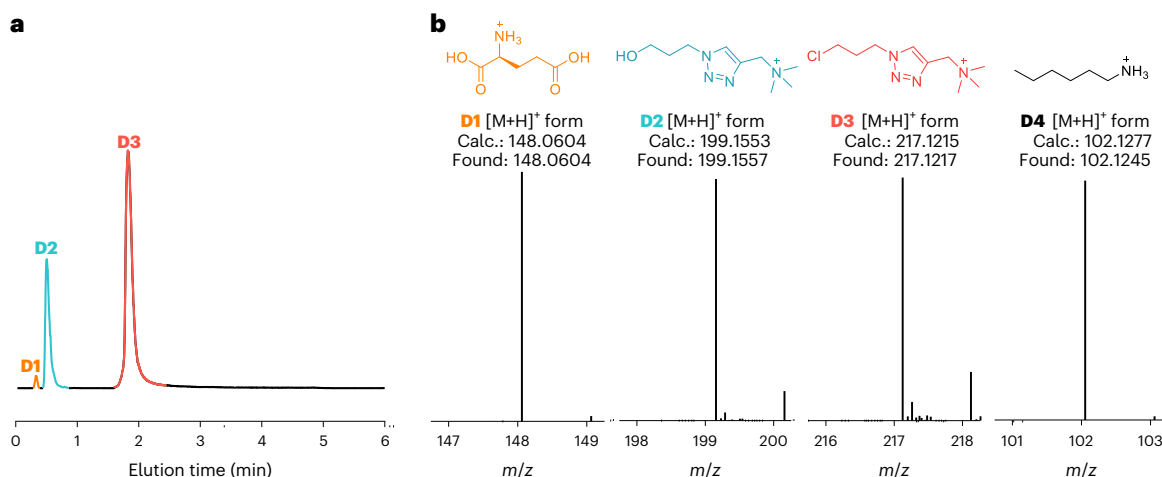
Fig. 6 | Acid degradation of PPILs. a,b, Degradation analysis of PPILs by LC–MS (positive ESI): trace map (**a**) and chemical structures (**b**) of the observed products. Calc., calculated.

($V_{DCM}/V_{pH\,7\,phosphate\,buffer}$ = 95%/5%) was then performed with a monomer to macroinitiator ratio $[M]_0/[I]_0$ varying from 200 to 950, and the obtained MWs matched the expected MW with $Đ$ < 1.05 (Fig. 3b and Supplementary Fig. 28). Post-modification to PPILs (Supplementary Scheme 3) was confirmed by NMR (Supplementary Figs. 29–32). The right-handed α-helix was intact after functionalization based on ATR-FTIR and CD spectra (Supplementary Fig. 33). Five helical polymers (Fig. 3c, L-50, L-233, L-498, L-768, L-925) showed similar $T_{d,5\%}$ and T_g increased modestly from 297 K to 304 K with increasing MW (Supplementary Figs. 34 and 35).

Longer helices promote higher conductivity

In contrast to random coil PILs[36,40–43], the ionic conductivity of helical PPILs increased with increasing DP (Fig. 3d,e, Supplementary Figs. 36–39, Supplementary Tables 1 and 2) despite a 5 K T_g increase relative to L-50. The T_g-normalized ionic conductivity of the longest L-925 was 5–50 times higher than that of L-50, going from 0.75 to 1.0 T_g/T (Fig. 3f). L-925 was ultimately 65 times more conductive than LD-50, illustrating the combined effect of secondary structure and peptide length—longer helices more efficiently transport ions along the backbone. The conductivity of the longest helix exceeds 10^{-3} S cm^{-1} at high temperatures, which is comparable to the conductivity of salt-in-polymer systems[43] despite it being a single-ion conductor. Future approaches to reduce T_g through copolymerization or achieve synergistic effects of sequence[44] can increase the room temperature conductivity.

The helix macrodipole increases with DP[45], which increases the dielectric constant beyond values reported for previous PILs[46] to create a more favourable environment for ion solvation and conduction (Fig. 4a,b). Helices oriented in the direction of the field will show enhanced transport, whereas those perpendicular to the field will show no effect. The persistence lengths (l_p) of α-helical peptides are substantially higher than those of random coil polymers in solution; for example, α-helical poly-L-lysine has $l_p \approx 15$–20 nm compared with random coil polymers which are ~1 nm or less[47]. Separate simulations indicate that the l_p of helical peptides is around 100 nm (ref. 48). The l_p of poly(γ-benzyl-L-glutamate) in the melt was reported as 1–2 nm through dielectric analysis of the dipole moment of the helix, but was not compared to an analogous random coil[49]. Charge, solvent and side chain will dictate the precise value of l_p in helical PILs, but it is still expected to be higher than for an analogous random coil. Even with defects or bending along a helical backbone, the macrodipole will still increase the dielectric constant and direct transport in a more efficient manner. Techniques such as neutron scattering will be critical to probe solid-state l_p or the correlation lengths of PPILs.

The five L-DP materials have identical chemical formulas, charges and secondary structures, and thus the increased ionic conductivity is due to (1) the presence of a helix and (2) increasing helix length. LD-50 has a similar conductivity to previous random coil ammonium PILs of various DPs (Fig. 4c)[40,50]. SAXS/WAXS measurements (Fig. 4d and Supplementary Fig. 40) show an invariance in the amorphous halo (q_1, -13.5 nm^{-1}), while the intensity and d-spacing of q_2 increased with increasing DP as the ions are correlated over longer length scales, leading to enhanced scattering and higher conductivity.

Liquid crystallinity at PPIL surfaces

Helical peptides can form liquid crystalline (LC) phases which would impact conductivity. Polarized optical microscopy (POM) and grazing incidence X-ray scattering (GISAXS and GIWAXS) were performed, and POM showed no LC order for the random coils or the shortest L-50 helical sample (Fig. 5a). Longer helices show LC textures, and for L-233 and L-498 a non-reversible transition to isotropic is observed above 120 °C (Supplementary Figs. 41 and 42) indicating the order is induced by hot-pressing. L-768 and L-925 show stable LC texture up to 150 °C, supporting the picture of rigid helices that persist and drive LC assembly. GISAXS shows a scattering peak at $q \approx 0.2$ nm^{-1} for L-233 to L-925, but not for L-50 or LD-50, consistent with POM (Fig. 5b and Supplementary Figs. 43 and 44). WAXS and GIWAXS show no discernible differences (Supplementary Fig. 45) and indicate no crystallinity. Calorimetry reveals no LC transition in any of the samples, indicating that order is present only at the surface of the films which are transparent (Fig. 1a). Future work optimizing LC orientation will lead to further enhancements in the ionic conductivity along the helix direction.

On-demand degradation of PPILs

Polymers are difficult to degrade, but PPILs possess amide and ester bonds that are acid-, base- and enzyme-degradable. In 6 M HCl at 110 °C, PPILs completely degraded after 1 day to four degradation products detected by liquid chromatography–mass spectrometry (LC–MS, Fig. 6) and ^{1}H NMR (Supplementary Figs. 46–49), including protonated hexylamine, glutamic acid and chlorinated derivatives from the side chains. Future work will investigate milder pathways, including enzyme degradation. All samples are stable over a 6 V window (Supplementary Figs. 50 and 51).

Helical ionic peptides are a powerful new platform for solid electrolytes with improved conductivity and stability. The helices resist conformational changes up to 200 °C, allowing for higher conductivity than unstable random coil analogues, and are stable over a 6 V window. Conductivity can be further enhanced by increasing the helix length

which increases the macrodipole, dielectric constant and ion–ion correlations. PPILs are readily degraded in acid for recyclability. The PPIL approach is readily generalizable to other ion pairs and functional groups via click chemistry. This work not only paves the way for future mechanistic studies but also the design of next-generation stable, recyclable and high-performance electrolytes.

Online content

Any methods, additional references, Nature Portfolio reporting summaries, source data, extended data, supplementary information, acknowledgements, peer review information; details of author contributions and competing interests; and statements of data and code availability are available at https://doi.org/10.1038/s41563-024-01966-1.

References

1. Sun, H. T. et al. Hierarchical 3D electrodes for electrochemical energy storage. *Nat. Rev. Mater.* **4**, 45–60 (2019).
2. Sun, Y. L., Liu, B., Liu, L. Y. & Yan, X. B. Ions transport in electrochemical energy storage devices at low temperatures. *Adv. Funct. Mater.* **32**, 2109568 (2022).
3. Xiao, K., Jiang, L. & Antonietti, M. Ion transport in nanofluidic devices for energy harvesting. *Joule* **3**, 2364–2380 (2019).
4. Chen, J. et al. Localized electrons enhanced ion transport for ultrafast electrochemical energy storage. *Adv. Mater.* **32**, e1905578 (2020).
5. Yan, C. et al. Engineering 2D nanofluidic Li-ion transport channels for superior electrochemical energy storage. *Adv. Mater.* **29**, 1703909 (2017).
6. Lin, P. & Yan, F. Organic thin-film transistors for chemical and biological sensing. *Adv. Mater.* **24**, 34–51 (2012).
7. Jentsch, T. J. VRACs and other ion channels and transporters in the regulation of cell volume and beyond. *Nat. Rev. Mol. Cell Biol.* **17**, 293–307 (2016).
8. Ratner, M. A. & Shriver, D. F. Ion-transport in solvent-free polymers. *Chem. Rev.* **88**, 109–124 (1988).
9. Armand, M. & Tarascon, J. M. Building better batteries. *Nature* **451**, 652–657 (2008).
10. Shen, C. T., Zhao, Q. J., Shan, N. S., Jing, B. B. & Evans, C. M. Conductivity–modulus–T_g relationships in solvent-free, single lithium ion conducting network electrolytes. *J. Polym. Sci.* **58**, 2376–2388 (2020).
11. Bouchet, R. et al. Single-ion BAB triblock copolymers as highly efficient electrolytes for lithium-metal batteries. *Nat. Mater.* **12**, 452–457 (2013).
12. Sun, C. G. et al. Fast lithium ion transport in solid polymer electrolytes from polysulfide-bridged copolymers. *Nano Energy* **75**, 104976 (2020).
13. Sharon, D. et al. Intrinsic ion transport properties of block copolymer electrolytes. *ACS Nano* **14**, 8902–8914 (2020).
14. Liu, D. et al. Enhancing ionic conductivity in tablet–bottlebrush block copolymer electrolytes with well-aligned nanostructures via solvent vapor annealing. *J. Mater. Chem. C* **10**, 4247–4256 (2022).
15. Jia, D. et al. Multifunctional polymer bottlebrush-based gel polymer electrolytes for lithium metal batteries. *Mater. Today Nano* **15**, 100128 (2021).
16. Deng, C. T. et al. Role of molecular architecture on ion transport in ethylene oxide-based polymer electrolytes. *Macromolecules* **54**, 2266–2276 (2021).
17. Evans, C. M., Bridges, C. R., Sanoja, G. E., Bartels, J. & Segalman, R. A. Role of tethered ion placement on polymerized ionic liquid structure and conductivity: pendant versus backbone charge placement. *ACS Macro Lett.* **5**, 925–930 (2016).
18. Sangoro, J. R. et al. Decoupling of ionic conductivity from structural dynamics in polymerized ionic liquids. *Soft Matter* **10**, 3536–3540 (2014).
19. Jones, S. D. et al. Design of polymeric zwitterionic solid electrolytes with superionic lithium transport. *ACS Cent. Sci.* **8**, 169–175 (2022).
20. Leigh, T. & Fernandez-Trillo, P. Helical polymers for biological and medical applications. *Nat. Rev. Chem.* **4**, 291–310 (2020).
21. Ekladious, I., Colson, Y. L. & Grinstaff, M. W. Polymer–drug conjugate therapeutics: advances, insights and prospects. *Nat. Rev. Drug Discov.* **18**, 273–294 (2019).
22. Gao, Y. et al. Winding-locked carbon nanotubes/polymer nanofibers helical yarn for ultrastretchable conductor and strain sensor. *ACS Nano* **14**, 3442–3450 (2020).
23. Wang, M. X. et al. Conductance-stable and integrated helical fiber electrodes toward stretchy energy storage and self-powered sensing utilization. *Chem. Eng. J.* **457**, 141164 (2023).
24. Liu, Y. S. et al. Controllable synthesis of Co@CoO$_x$/helical nitrogen-doped carbon nanotubes toward oxygen reduction reaction as binder-free cathodes for Al–air batteries. *ACS Appl. Mater. Interfaces* **12**, 16512–16520 (2020).
25. Zhao, M. Q. et al. Hierarchical vine-tree-like carbon nanotube architectures: in-situ CVD self-assembly and their use as robust scaffolds for lithium–sulfur batteries. *Adv. Mater.* **26**, 7051–7058 (2014).
26. Jiang, Y. J. et al. 'Metaphilic' cell-penetrating polypeptide–vancomycin conjugate efficiently eradicates intracellular bacteria via a dual mechanism. *ACS Cent. Sci.* **6**, 2267–2276 (2020).
27. Jiang, Y., Chen, Y., Song, Z., Tan, Z. & Cheng, J. Recent advances in design of antimicrobial peptides and polypeptides toward clinical translation. *Adv. Drug. Deliv. Rev.* **170**, 261–280 (2021).
28. Nguyen, T. P. et al. Polypeptide organic radical batteries. *Nature* **593**, 61–66 (2021).
29. Lightfoot, P., Mehta, M. A. & Bruce, P. G. Crystal structure of the polymer electrolyte poly(ethylene oxide)$_3$:LiCF$_3$SO$_3$. *Science* **262**, 883–885 (1993).
30. Ma, Y. A., Shen, Y. & Li, Z. B. Different cell behaviors induced by stereochemistry on polypeptide brush grafted surfaces. *Mater. Chem. Front.* **1**, 846–851 (2017).
31. Papadopoulos, P., Floudas, G., Klok, H. A., Schnell, I. & Pakula, T. Self-assembly and dynamics of poly(γ-benzyl-L-glutamate) peptides. *Biomacromolecules* **5**, 81–91 (2004).
32. Kricheldorf, H. R. & Mueller, D. Secondary structure of peptides. 3. Carbon-13 NMR cross polarization/magic angle spinning spectroscopic characterization of solid polypeptides. *Macromolecules* **16**, 615–623 (1983).
33. Tsutsumi, A. et al. Relaxation phenomena of poly-γ-benzyl-L-glutamate, poly-γ-methyl-L-glutamate, and copoly(γ-methyl-L-glutamate, γ-benzyl-L-glutamate). *J. Macromol. Sci., B* **8**, 413–430 (1973).
34. Evans, C. M., Sanoja, G. E., Popere, B. C. & Segalrnan, R. A. Anhydrous proton transport in polymerized ionic liquid block copolymers: roles of block length, ionic content, and confinement. *Macromolecules* **49**, 395–404 (2016).
35. Drozd-Rzoska, A., Rzoska, S. J. & Starzonek, S. New paradigm for configurational entropy in glass-forming systems. *Sci. Rep.* **12**, 3058 (2022).
36. Heres, M. et al. Ion transport in glassy polymerized ionic liquids: unraveling the impact of the molecular structure. *Macromolecules* **52**, 88–95 (2019).
37. Cheng, S. J. et al. Ionic aggregation in random copolymers containing phosphonium ionic liquid monomers. *J. Polym. Sci. A1* **50**, 166–173 (2012).
38. Hemp, S. T. et al. Comparing ammonium and phosphonium polymerized ionic liquids: thermal analysis, conductivity, and morphology. *Macromol. Chem. Phys.* **214**, 2099–2107 (2013).

39. Xia, Y. C. et al. Accelerated polymerization of *N*-carboxyanhydrides catalyzed by crown ether. *Nat. Commun.* **12**, 732 (2021).

40. Fan, F. et al. Effect of molecular weight on the ion transport mechanism in polymerized ionic liquids. *Macromolecules* **49**, 4557–4570 (2016).

41. Zhao, Q. J. & Evans, C. M. Effect of molecular weight on viscosity scaling and ion transport in linear polymerized ionic liquids. *Macromolecules* **54**, 3395–3404 (2021).

42. Keith, J. R., Mogurampelly, S., Aldukhi, F., Wheatle, B. K. & Ganesan, V. Influence of molecular weight on ion-transport properties of polymeric ionic liquids. *Phys. Chem. Chem. Phys.* **19**, 29134–29145 (2017).

43. Timachova, K., Watanabe, H. & Balsara, N. P. Effect of molecular weight and salt concentration on ion transport and the transference number in polymer electrolytes. *Macromolecules* **48**, 7882–7888 (2015).

44. Han, S. et al. Sequencing polymers to enable solid-state lithium batteries. *Nat. Mater.* **22**, 1515–1522 (2023).

45. Wada, A. Dielectric properties of polypeptide solutions. II. Relation between the electric dipole moment and the molecular weight of α helix. *J. Chem. Phys.* **30**, 328–329 (1959).

46. Choi, U. H. et al. Role of chain polarity on ion and polymer dynamics: molecular volume-based analysis of the dielectric constant for polymerized norbornene-based ionic liquids. *Macromolecules* **53**, 10561–10573 (2020).

47. Wilcox, K. G., Dingle, M. E., Saha, A., Hore, M. J. A. & Morozova, S. Persistence length of α-helical poly-L-lysine. *Soft Matter* **18**, 6550–6560 (2022).

48. Choe, S. & Sun, S. X. The elasticity of α-helices. *J. Chem. Phys.* **122**, 244912 (2005).

49. Papadopoulos, P. et al. Thermodynamic confinement and α-helix persistence length in poly(γ-benzyl-L-glutamate)-*b*-poly(dimethyl siloxane)-*b*-poly(γ-benzyl-L-glutamate) triblock copolymers. *Biomacromolecules* **7**, 618–626 (2006).

50. Zhao, Q. J., Bennington, P., Nealey, P. F., Patel, S. N. & Evans, C. M. Ion specific, thin film confinement effects on conductivity in polymerized ionic liquids. *Macromolecules* **54**, 10520–10528 (2021).

Methods

All detailed experimental procedures and characterization of compounds can be found in the Supplementary Information.

Data availability

The authors declare that all data supporting the findings of this study are available within the paper and the Supplementary Information. The raw numbers for charts and graphs are available in the provided Source Data file whenever possible. Additional images are available from the corresponding author upon reasonable request. Source data are provided with this paper.

Author contributions

C.M.E conceived of using the helix to enhance conductivity, and Y.C and T.X. conceived of the polymer electrolyte design and synthesis. Solid ^{13}C NMR was conducted by S.J. Dielectric spectroscopy was conducted by C.C. Y.C. and C.M.E. wrote the manuscript with contributions and critical feedback from T.X., C.C., S.J., J.C. and P.V.B. All authors discussed the results and commented on the manuscript.

Competing interests

The authors declare no competing interests.

Additional information

Supplementary information The online version contains supplementary material available at https://doi.org/10.1038/s41563-024-01966-1.

Correspondence and requests for materials should be addressed to Christopher M. Evans.

Peer review information *Nature Materials* thanks Darrin Pochan and the other, anonymous, reviewer(s) for their contribution to the peer review of this work.

Reprints and permissions information is available at www.nature.com/reprints.